6. Fe/Tb multilayers with diamagnetic layers

As shown previously by MOKE investigations the interfaces exert a large influence on the magnetization reversal behavior and strongly contribute to the PMA of the MLs. As a consequence of the different atomic radii and surface energies of Fe and Tb, respectively, different structures of top and bottom interfaces are expected. This was in fact corroborated by means of in situ resistance measurements, where an asymmetry in resistance of a Tb/Fe/Tb trilayer [Dufo91] was found. In particular CEMS studies of on the probe layers of ^{57}Fe showed that the top interfaces are smooth and composed of α-Fe, whereas the bottom interfaces are rough and merely consist of amorphous Fe [Tapp94, Rich96a]. Besides, recent in situ CEMS measurements on bilayers of Tb-on-Fe (top) and Fe-on-Tb (bottom) revealed that primarily the top interface induces the PMA of α-Fe at low temperature [Scho94a].

In order to investigate the influence of the individual interfaces on the PMA and magnetization reversal process either the top or bottom interfaces of the individual Fe layers were replaced by diamagnetic yttrium or silver blocking layers and investigated by using torque magnetometer, MOKE and SQUID magnetometry, respectively.

In Section 6.1. report on torque investigations on the Tb/bcc-Fe multilayers with and without diamagnetic Y blocking layers, [Tb(1.4)/Fe(5.0)/Y(1.2 nm)]$_{10}$ (=Y1, Fe-on-Tb), [Y(1.2)/Fe(5.0)/Tb(1.4 nm)]$_{10}$ (=Y2, Tb-on-Fe) and [Tb(2.6)/Fe(5.0 nm)]$_{10}$ (=Y3), will be presented. Here structural influences of Tb can be separated from magnetic ones via Y owing to its lack of 4f moments. In order to understand the measured TCs a model calculation based on the coherent rotation model of Stoner and Wohlfarth (SW) [Ston48] was performed. The TCs are described within the framework of two-layer models being uncoupled at higher temperature (T > 200 K) and coupled at low temperature (T ≤ 50 K). In particular the cone structure of the Fe moments in Y3 due to antiferromagnetically coupling between Fe and Tb moments will be discussed. In addition the anisotropy constants of the samples and their temperature dependence determined will be presented.

In Section 6.2. the effects of the two different interfaces, Fe-on-Tb and Tb-on-Fe, on the magnetization reversal and the PMA studied by MOKE and SQUID magnetometry will be discussed. They were measured on the Tb/bcc-Fe multilayers with and without diamagnetic

Ag blocking layers, [Tb(1.4)/Fe(3.5)/Ag(5.0 nm)]$_{10}$ (=Ag1, Fe-on-Tb), [Ag(5.0)/Fe(3.5)/ Tb(1.4 nm)]$_{10}$ (=Ag2, Tb-on-Fe) and [Tb(1.4)/Fe(3.5 nm)]$_{10}$ (=Ag3). Analysis of the polar Kerr hysteresis loops obtained at various wavelengths is performed. It is observed that ε_K measured at intermediate wavelengths, 525 - 575 nm, can be described by a linear combination of the hysteresis loops at short-wavelengths (~ 300 nm) and long-wavelengths (600 - 700 nm). In particular element specific selectivity of different Fe modifications, α-, bulk a-Fe and uncoupled a-Fe is encountered within the observed by polar Kerr spectra and hysteresis loops.

6.1. Fe/Tb multilayers with Y layers

6.1.1. Torque measurements

Fig. 6.1 and 2 show the measured TCs of Y1 and Y2 at different temperatures, 15 K $\leq$ T $\leq$ 300 K, respectively. At the first glance both samples behave similarly with respect to the overall angular dependence and to its change with decreasing temperature. At T $\geq$ 200 K the observed TCs are typical of a sample with in-plane anisotropy [Pech91]. An increasing torque, τ, is exerted to the film when rotating **H** out of the film plane. The sign of τ is defined by the sense of rotation, counterclockwise (CCW) or clockwise (CW). $|\tau|$ maximises to a value τ_{max} as α $\rightarrow$ 90° and sawtooth-like changes sign at $\alpha > 90°$ owing to the flip of the in-plane component of **M$_S$** from **e** to **e'** (Fig. 4.2).

With decreasing temperature the amplitude of τ decreases. This behavior is attributed to a decrease of the in-plane anisotropy, or, in other words, to an increase of the PMA. A model calculation will be presented in Section 6.1.2. Here we remark that the decrease of τ_{max} observed within the interval $0° < \alpha < 90°$ between T = 300 and 100 K, $\Delta\tau = \{\tau_{max}(300$ K) - $\tau_{max}(100$ K)$\}/\tau_{max}(300$ K), is about 20% larger in Y2 ($\Delta\tau = 0.4$) than in Y1 ($\Delta\tau = 0.32$). This indicates that the smooth Tb-on-Fe interfaces develop significantly larger PMA than the rough Fe-on-Tb interfaces when cooling to below the Curie temperature of crystalline Tb, T_C(Tb) = 219.3 K [Elli72].
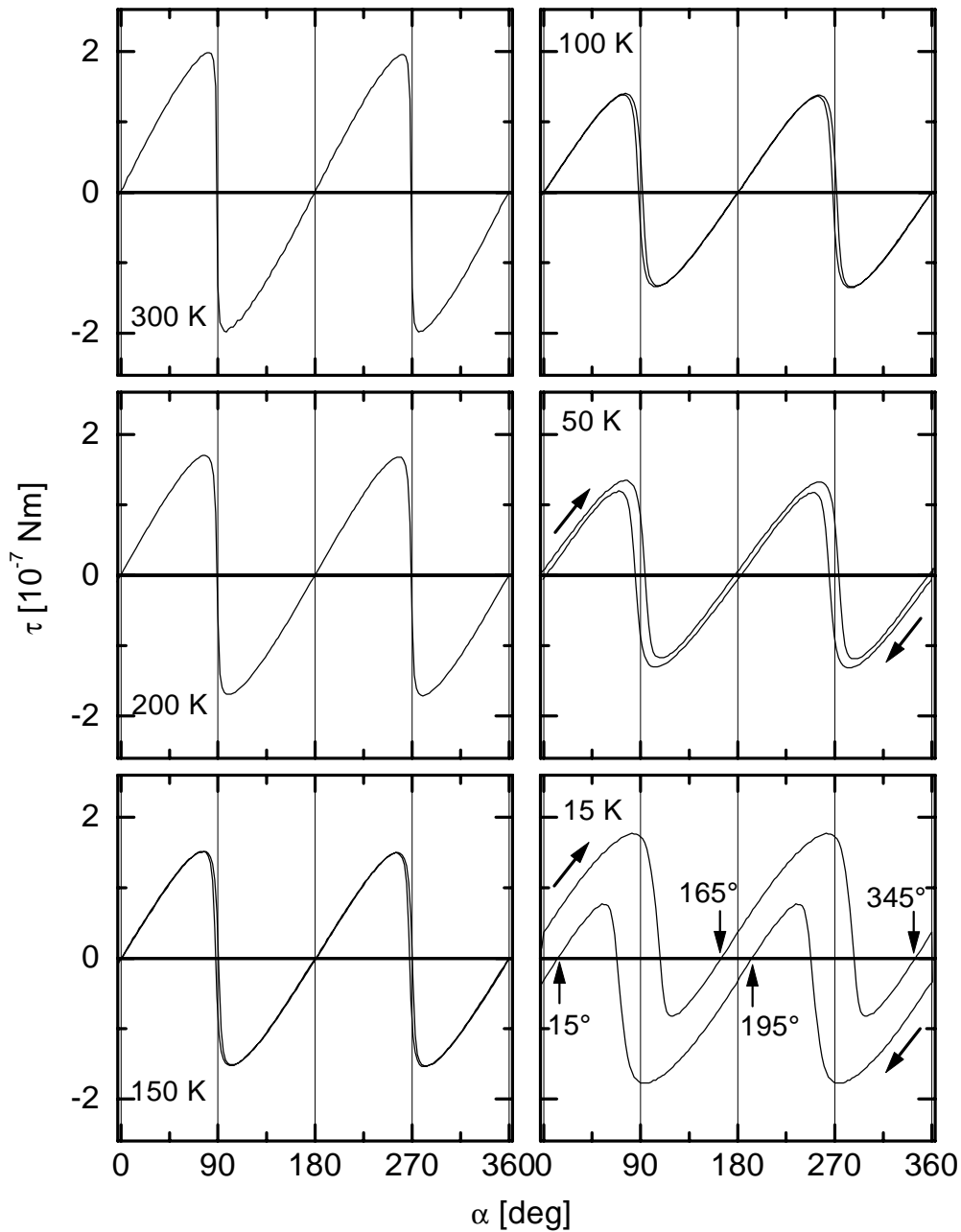
Fig. 6.1: Torque curves of Y1 at different temperatures, 15 K ≤ T ≤ 300 K, obtained with H = 0.72 MA/m. The film plane lies perpendicularly to the plane of field-rotation. Arrows indicate the directions of the field-rotation (T = 15 and 50 K) and the effective cone angles (T = 15 K, see text).

The TCs of Y1 (Fig. 6.1) show not only a decrease of τ but also rotational hysteresis (RH) near $\alpha = 90$ and 270° upon cooling to T = 100 K. Such a RH is, in terms of a coherent rotation model [Ston48], unexpected for an easy plane system (see Section 6.1.2.). Probably secondary intraplanar anisotropy or some kind of in-plane coercivity is encountered with decreasing T. It gives rise to domain pinning during magnetization reversal. Presumably this is due to the in-

plane counterparts of the randomly distributed local anisotropy axes within the amorphous TbFe alloys [Albe78] contained in the rough Fe-on-Tb interfaces. Remarkably, RH of this kind is much weaker in Y2 (Fig. 6.2) owing to reduced alloying in the smooth Tb-on-Fe interfaces.
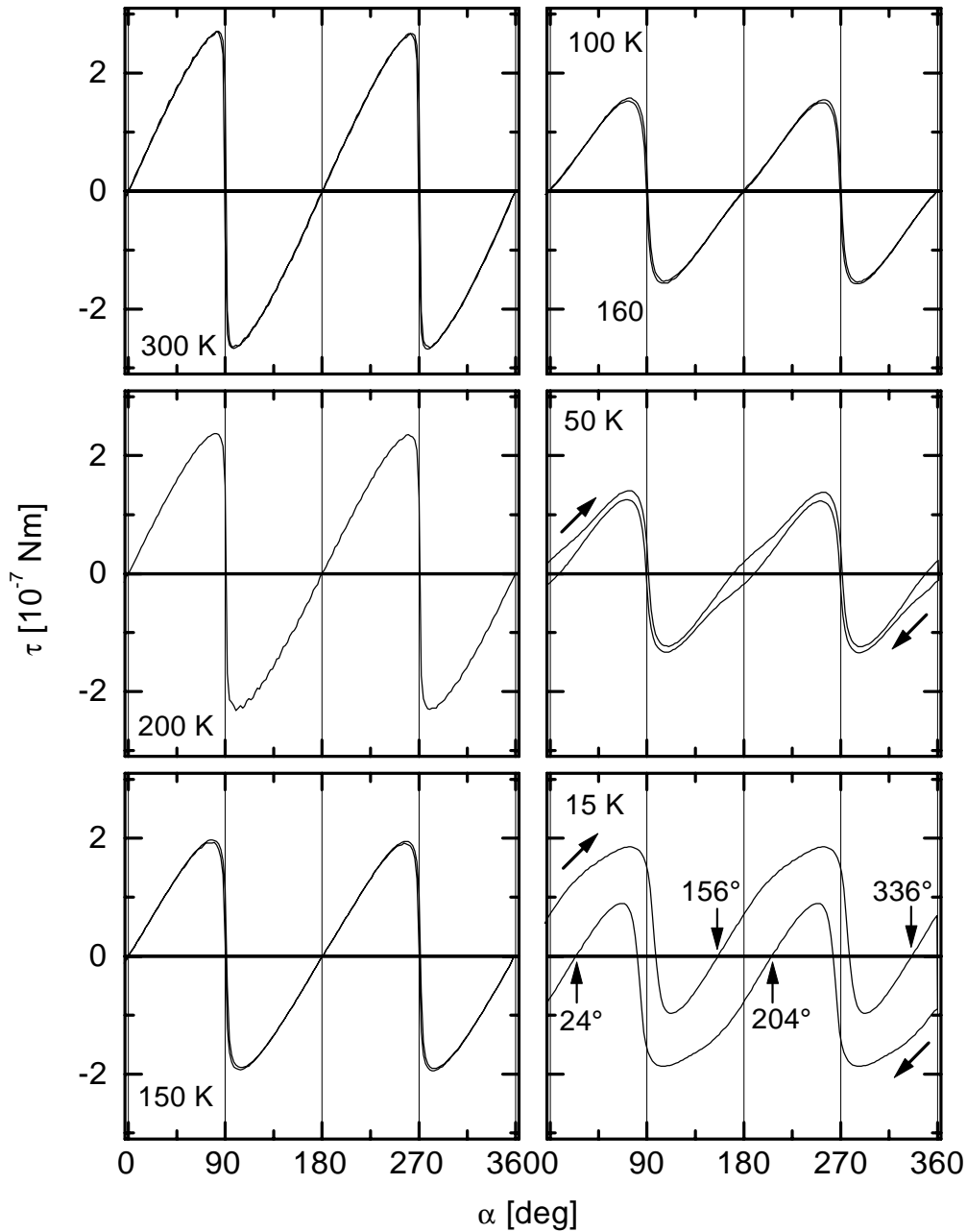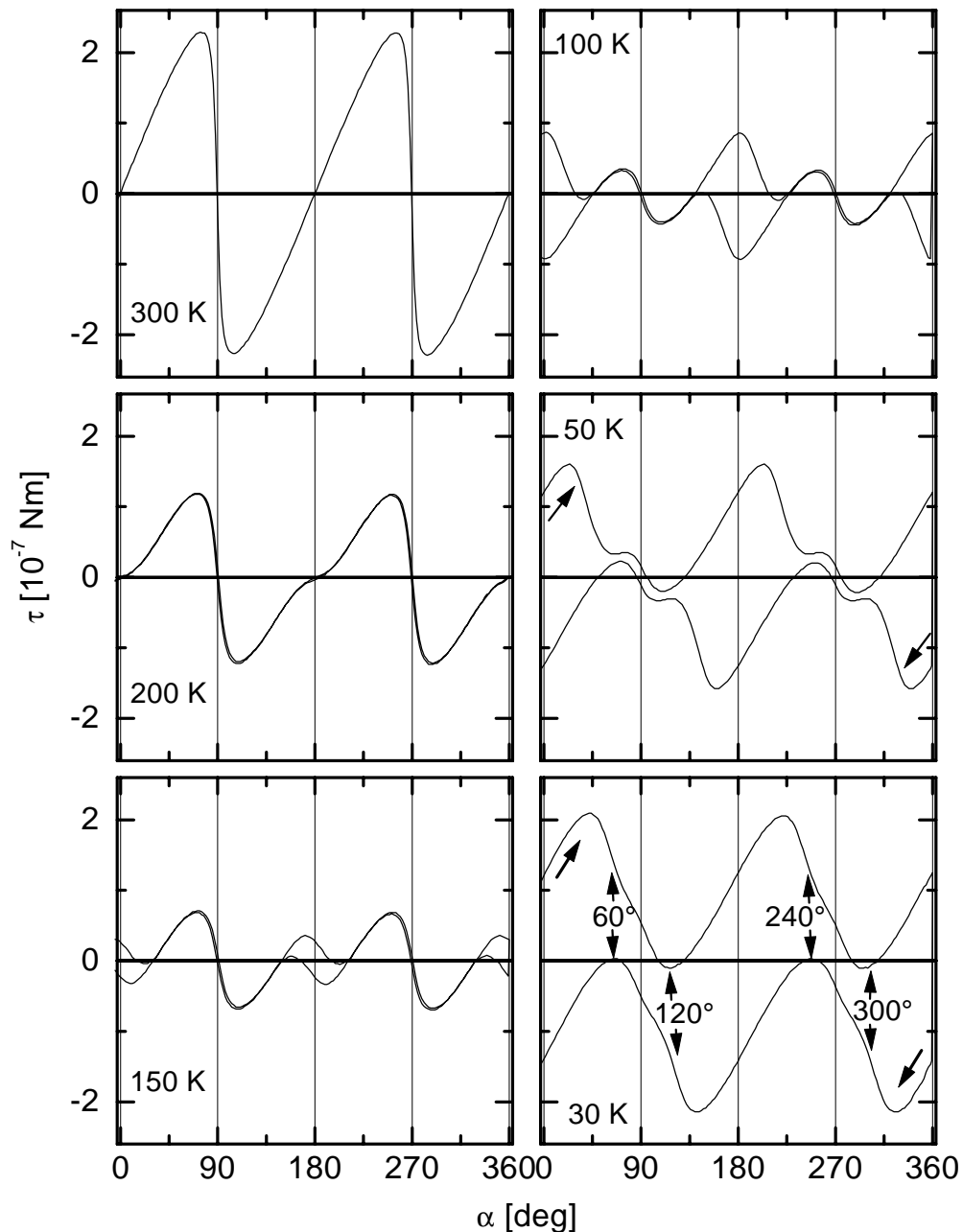

Fig. 6.2: Torque curves of Y2 at different temperatures, 15 K ≤ T ≤ 300 K, obtained with H = 0.72 MA/m. The film plane lies perpendicularly to the plane of field-rotation. Arrows indicate the directions of the field-rotation (T = 15 and 50 K) and the effective cone angles (T = 15 K, see text).

At a closer look to the TC of Y2 a decrease of the slope is observed in the vicinity of $\alpha = 0$, 180°, 360°, ⋯ upon cooling to T = 100 K (Fig. 6.2). This is a first hint at magnetic heterogeneity to be considered within the bilayers. As will be shown in Section 6.1.2. within an uncoupled two-layer model the S-shape of the TC in the vicinity of e.g. $\alpha = 180°$ can be understood as a superposition of two TCs with opposite character. In addition to the dominant TC of in-plane magnetized bulk α-Fe a weak TC, opposite in sign and phase-shifted by 90°, has to be considered. It is due to the Fe/Tb interfaces, which gain increasingly PMA as T is lowered to below $T_C(Tb)$.

In the low T-region, T ≤ 50 K, the RH of the two samples, Y1 and Y2, is no longer restricted to the vicinity of $\alpha = 90, 270°$, ⋯, but extends over the entire angular range, $0° \leq \alpha \leq 360°$ (Fig. 6.1 and 2). The curves for CCW and CW rotation of **H** are substantially shifted against one another. Similar, albeit uncommented effects were found by Krishnan et al. [Kris88] on amorphous FeTb alloys at low temperatures. Owing to the well-known ferrimagnetic coupling between Tb and Fe spins [Camp72] conical spin ordering takes place, where the Fe spins are preferentially aligned under intermediate polar angles, $0 < \theta_1 < 90°$ [Eyme88]. Hence, zero mechanical torque should be observed whenever the field is parallel to the oblique easy direction, $\alpha \approx 90° \pm \theta_1$. This can be explained within the framework of an effective one-layer model exhibiting conical spin structure as discussed in Section 6.1.3.

Fig. 6.3 shows the TCs of the multilayer Y3, which lacks any blocking layers of Y. It reveals similar temperature dependencies as found in the case of Y2. The angular regions around $\alpha = 0$ and 180° are characterized first by reduced slopes at T = 200 K and then by the onset of RH at T ≤ 150 K. These features appear at temperatures being about 100 K higher than for the corresponding situations observed on Y2 (Fig. 6.2). In addition, the torque peaks in the vicinity of $\alpha = 90$ and 270° become drastically reduced at T < 150 K. When comparing the torque amplitudes near 90 and 180°, obviously the contribution of PMA dominates at T ≤ 100 K. This behavior strongly hints at mutual coupling of all interfaces, top and bottom, by virtue of the magnetized Tb layers. In addition, enhanced PMA within the α-Fe layers is expected owing to dipolar coupling between adjacent bilayers [Suna86]. Strong PMA occurring in Tb/Fe multilayers without blocking layers is a well-known low-T feature as confirmed e. g. by measurements of hysteresis cycles with MOKE and SQUID techniques [Kim97].

Fig. 6.3: Torque curves of Y3 at different temperatures, 30 K ≤ T ≤ 300 K, obtained with H = 0.72 MA/m. The film plane lies perpendicularly to the plane of field-rotation. Arrows indicate the directions of the field-rotation (T = 30 and 50 K) and the effective cone angles (T = 30 K, see text).

Peculiarly, however, upon further cooling to T = 30 K the TC does not become symmetric around the normal directions, α = 90 and 270°. We observe sawtooth-like curves, the zeros of which are shifted by about ± 30° with respect to the expected positions. Again, conical spin structure has to be taken into account. Details within an effective one-layer model will be presented in Section 6.1.3.

6.1.2. Uncoupled two-layer model

The TCs observed on Y1, Y2 and Y3 (T > 100 K) can be modeled by a computer simulation based on a two-layer model involving two different anisotropies, in-plane in the bulk α-Fe and out-of-plane in the interfaces between Fe and Tb layers, respectively. The magnetization reversal process is described by the S-W coherent rotation model [Ston48] assuming homogeneous magnetization within each layer. The free energy of the two-layer system in an applied field **H,** involving first-order uniaxial anisotropies and interlayer coupling, reads

$$
\begin{aligned}
E = \sum_{i=A,B} V_i \cdot K_{eff}^i \cdot \sin^2(\alpha - \delta_i) - \sum_{i=A,B} \mu_0 \cdot V_i \cdot M_S^i \cdot H \cdot \cos\delta_i \\
- \Lambda^* \cdot S \cdot M_S^A \cdot M_S^B \cdot \cos(\delta_A - \delta_B).
\end{aligned}
\tag{6. 1}
$$

V_i and M_S^i are the volumes and the saturation magnetizations of the layers i = A and B, respectively. By definition layer A consists of bulk Fe, whereas layer B includes both bulk Tb and the adjacent ferrimagnetically coupled monolayers of Fe. δ_i and α represent the angles between M_S^i and **H**, and **H** and **e**, respectively (Fig. 4.4). The anisotropy constants K_{eff}^i account for both the uniaxial anisotropy constants K_u^i and the shape anisotropy $\frac{\mu_0}{2} \cdot (N_\perp - N_\parallel) \cdot M_S^2$, where μ_0, $N_\perp$ and $N_\parallel$ are permeability of vacuum, the demagnetizing factors perpendicular and parallel to the film plane, respectively. In the following we shall assume $K_{eff}^A > 0$ and $K_{eff}^B < 0$, i. e. effective planar and perpendicular anisotropy energy densities of the layers A and B, respectively. Λ^* describes the exchange coupling between the Fe atoms at the interface (area S) and the α-Fe in the bulk. Its sign depends on the magnitude of the Tb moments in layer B and may switch from positive to negative upon lowering the temperature. Below we shall consider the limiting cases of weak ($M_B \approx 0$) and strong coupling ($M_B \neq 0$), which seem approximately to apply to the cases of negligible (T > 200 K), and fully active interlayer coupling at T ≤ 50 K.

Minimization of E with respect to the angles δ_i leads to the equilibrium positions of the magnetization vectors. Necessary conditions are

$$\frac{\partial E}{\partial \delta_A} = -k_A \cdot \sin 2(\alpha - \delta_A) + \mu_0 \cdot m_A \cdot H \cdot \sin \delta_A + \Lambda \cdot m_A \cdot m_B \cdot \sin(\delta_A - \delta_B) = 0 \qquad (6.2)$$

and

$$\frac{\partial E}{\partial \delta_B} = -k_B \cdot \sin 2(\alpha - \delta_B) + \mu_0 \cdot m_B \cdot H \cdot \sin \delta_B - \Lambda \cdot m_A \cdot m_B \cdot \sin(\delta_A - \delta_B) = 0, \qquad (6.3)$$

where the magnetic moments $m_A = V_A \cdot M_S^A$, $m_B = V_B \cdot M_S^B$, the anisotropy energies $k_A = V_A \cdot K_{eff}^A$, $k_B = V_B \cdot K_{eff}^B$ and the coupling constant $\Lambda = \dfrac{\Lambda^* \cdot S}{V_A \cdot V_B}$ are introduced.

The torques τ_i of layer i = A and B exerted by the external field H are given by:

$$\tau_A = \mu_0 \cdot m_A \cdot H \cdot \sin \delta_A = -\Lambda \cdot m_A \cdot m_B \cdot \sin(\delta_A - \delta_B) + k_A \sin 2(\alpha - \delta_A) \qquad (6.4)$$

and

$$\tau_B = \mu_0 \cdot m_B \cdot H \cdot \sin \delta_B = \Lambda \cdot m_A \cdot m_B \cdot \sin(\delta_A - \delta_B) + k_B \sin 2(\alpha - \delta_B) \qquad (6.5)$$

Let us first assume weak interlayer coupling, $\Lambda = 0$. Then by using the Eqs. (6. 4 and 5) the normalized torques may be written as

$$T_{A,B} = \frac{\tau_{A,B}}{k_{A,B}} = h_{A,B} \cdot \sin \delta_{A,B} = \sin 2(\alpha - \delta_{A,B}). \qquad (6.6)$$

where $h_{A,B} = \mu_0 \cdot m_{A,B} \cdot H / k_{A,B}$.

Solving the right-hand sides of Eq. (6. 6) independently for δ_A and δ_B one may calculate $T_{A,B}$ vs α numerically. Fig. 6.4 shows the calculated TCs for the individual layers A (a) and B (b) at various reduced fields, $0.3 \leq |h_{A,B}| \leq 2$, where $h_A > 0$ and $h_B < 0$ account for the different anisotropies involved. The shapes of the TCs are similar for both anisotropies except for a mutual shift by 90° and the lack of RH in the easy plane case (Fig. 6.4a). Moreover, the easy plane case does not show the transition to a $\sin\alpha$ behavior for $h_A < 0.5$. In the extreme cases of weak and strong relative anisotropy, $|h_{A,B}| > 1$ and < 0.5, the well-known sawtooth and sinusoidal TCs for easy-axis anisotropy, respectively, are obtained. The system with out-of-

plane anisotropy shows irreversible torque behavior around $\alpha = 0$ and $180°$ (Fig. 6.4b). In the following we shall try to model the measured TCs by best-fitting to linear combinations with appropriate amplitudes A, B and relative fields, $h_{A, B}$.
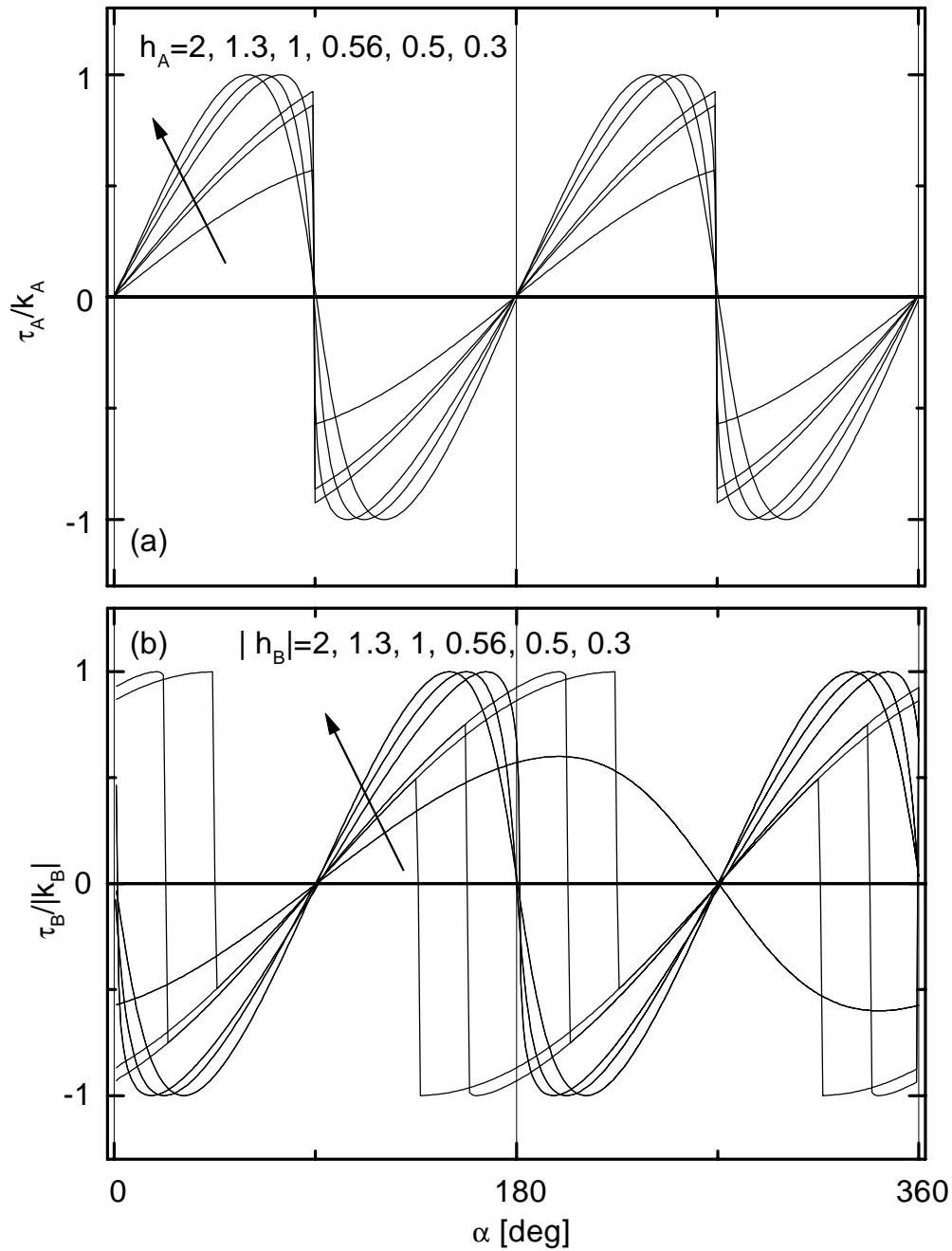

Fig. 6.4a: Normalized torque curves τ_A/k_A for easy plane oriented parallel to the film plane calculated for different values of $h = H/H_K$. b: Normalized torque curves $\tau_A/|k_B|$ for easy axis oriented perpendicular to the film plane calculated for different values of $|h| = H/H_K$.

Fig. 6.5a shows the results for the TC obtained on Y3 at $T = 200$ K (Fig. 6.3), which is best-fitted by the funtion $\tau(\alpha)/10^{-7}$ Nm $= 2.65 \cdot T_A(h_A = 1.3) + 0.55 \cdot T_B(|h_B| = 2)$, where T_A $(= \tau_A/k_A)$ and T_B $(= \tau_B/|k_B|)$ are normalized TCs as presented in Fig. 6.4. Obviously two slightly distorted $\sin 2\alpha$-like functions with different sign are superimposed, both of which indicate weak relative anisotropies. The dominating contribution is due to the in-plane anisotropic bulk
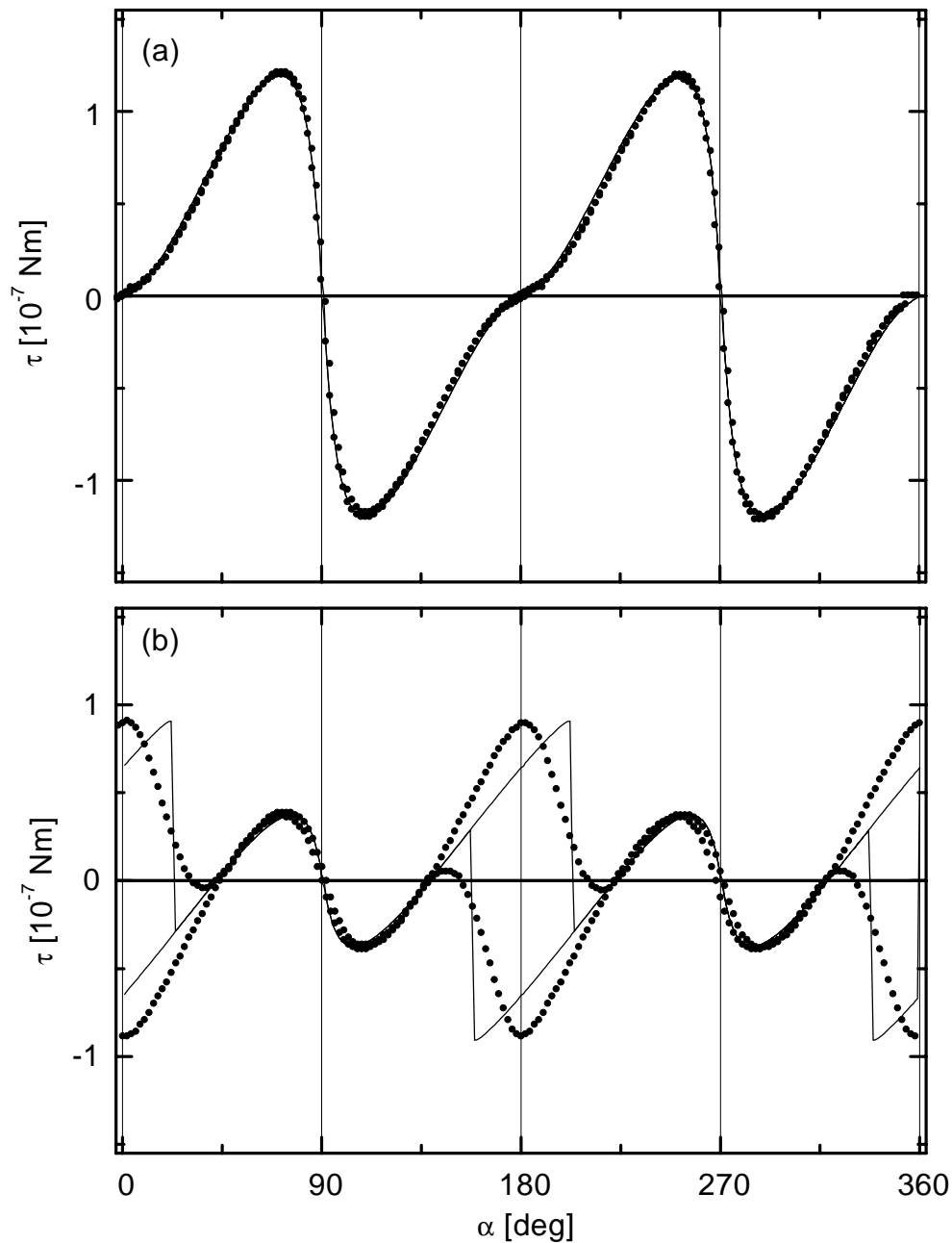

Fig. 6.5: Comparison of calculated (solid lines) with measured torque curves (solid circles) obtained on Y3 at T = 200 (a) and 100 K (b) (cf. Figure 6.3; see text).

α-Fe sublayers. Nevertheless, the counteracting contributions due to the PMA of the interfaces are noticeable. They give rise to flattening of $\tau(\alpha)$ in the vicinity of $\alpha \approx 0$ and 180°. In a similar way the TCs of Y1 (Fig. 6.1) and Y2 (Fig. 6.2) observed at $T \geq 100$ K may be modeled with non-hysteretic $T_{A, B}$ curves (Fig. 6.4) in the weak anisotropy limit.

Evaluation of the fitting parameters emerging from Fig. 6.5a, $h_A = 1.30$ and $\tau_A/k_A = 2.65$, yields $M_A = 1.14$ MA/m and $K_{eff} = 7.89 \cdot 10^5$ J/m³. In these figures layer A refers to α-Fe films, whose thickness $t_A = 4.25$ nm takes into account that 3 atomic Fe layers of thickness 0.75 nm are mixed into layer B [Scho94a]. M_A amounts to only about 2/3 of the bulk α-Fe value, M_{Fe} = 1.7 MA/m, although the value of the hyperfine field, $B_{HF} = 34$ T, hints at normal crystalline environment [Tapp98]. Very probably this discrepancy is due to the spin canting, which yields $\langle\theta\rangle = 44°$ in the α-Fe films [Tapp98]. Hence, only the planar component of the magnetization, $M_A = M_S \cdot \sin\langle\theta\rangle = 1.18$ MA/m, contributes to τ_A, whereas the perpendicular components seem to cancel each other. Spin canting due to induced PMA is also the reason for the small value of K_{eff}. It falls below the shape anisotropy, $\frac{\mu_0}{2} \cdot M_A^2 = 8.16 \cdot 10^5$ J/m³, by an amount of $K_U = 0.27 \cdot 10^5$ J/m³.

The TC measured on Y3 at $T = 100$ K is best-fitted by the function $\tau/10^{-7}$ Nm $= 1.05 \cdot T_A(h_A = 1.3) + 1.4 \cdot T_B(|h_B| = 0.56)$ as shown in Fig. 6.5b. The fit is satisfying except in the vicinity of $\alpha = 0$ and 180°, where RH occurs. Whereas the experimental data are smoothly varying, the calculated curves reveal abrupt jumps of τ at certain switching angles. These are in fact expected within the framework of the S-W model, which anticipates homogeneous magnetization, coherent spin rotation and sharp first-order jumps. Experimentally, however, these discontinuities seem to be smeared out by nucleation and multidomain processes. Anticipating the discussion of Section 6.1.3. we remark that part of the observed rounding has also to do with switching on a cone rather than collinear spin states as presumed in our simple two-layer model. As compared with the TC observed at $T = 200$ K (Fig. 6.5a) the relative amplitude of the A component, $k_A/(k_A + k_B)$, with planar anisotropy decreases from 83 to 43%. In parallel, the contribution due to the perpendicularly anisotropic B component, $k_B/(k_A + k_B)$, rises from 17 to 57%. Simultaneously it corresponds to a relatively large anisotropy constant as reflected by the weak relative field, $|h_B| = 0.56$. That is why hysteresis becomes noticeable at $T < 200$ K in the $\alpha = 0$ and 180° regions (Fig. 6.3).

Similar albeit much weaker splitting is observed in Y2 (Fig. 6.2) in the same angular regions, $\alpha = 0$ and $180°$, but at lower temperatures, $T \leq 50$ K. Since such a loop-like phenomenon is absent in Y1 (Fig. 6.1), we are inclined to attribute larger tendency towards PMA to Tb/Fe layer systems containing smooth Tb-on-Fe interfaces. This is corroborated by another signature indicating increasing contributions of PMA with decreasing temperature. When cooling Y1, Y2 and Y3 from $T = 300$ to 100 K, say (Fig. 6.1-3) we observe significant decreases of the sawtooth peak height at $\alpha \approx 90°$. Within the two-layer model this phenomenon can be explained by growing B-type contributions with inverted sign (Fig. 6.4b), which eventually may become hysteretic as $|h_B|$ becomes smaller than unity at low T (Y2 and Y3, see above).

6.1.3. Cone State Model

In the low T-regions, $T \leq 50$ K, the hysteresis starts to spread over the whole angular range, $0 \leq \alpha \leq 360°$, in all samples, Y1, Y2 and Y3 (Fig. 6.1-3). This phenomenon cannot be explained within the uncoupled two-layer model, Eq. (6. 6), where the hysteresis loops are expected to be localized around certain angles, $\alpha = 0, 90, 180°$ etc. Contrastingly, we find sawtooth-like TCs, where the CCW and the CW counterparts are shifted against one another along both the α and the τ axes. This feature appears most pronounced at very low temperatures, $T = 15 - 30$ K. For its explanation we consider the following conjectures: (i) strong magnetic coupling within bulk and interface sublayers invalidates the uncoupled two-layer model and reinstalls an effective one-layer model, (ii) strong ferrimagnetic coupling between Tb and Fe spins create sperimagnetic magnetization ordering with easy axes lying on cones under polar angles θ_1 and $\theta_2 = 180° - \theta_1$ with respect to the film normal. The latter property has frequently been verified on the Fe magnetization, $\mathbf{M}_A$, by using Mössbauer spectroscopy in both Tb/Fe alloys [Eyme88] and multilayers [Scho92, Tapp96]. Recently, low-T angles $\theta_1 \approx 30 - 35°$ have been determined in samples being similar to the present ones with Y replaced by Ag blocking layers [Mark98].

In order to describe the observed spin canting let us assume strong PMA within the interface such that $\mathbf{m}_B$ is always orientated perpendicularly to the film plane, $\alpha - \delta_B = \pm\pi/2$. Eq. (6. 1) then reads

$$E = k_A \cdot \cos^2 \theta_A + k_B - \mu_0 \cdot H \cdot [m_A \cdot \sin(\alpha + \theta_A) \pm m_B \cdot \sin\alpha] \mp \Lambda \cdot m_A \cdot m_B \cdot \cos\theta_A, \quad \text{(6. 7)}$$

where $\theta_A = \pi/2 + \delta_A - \alpha$ is the angle between $\mathbf{m}_A$ and $\tilde{\mathbf{n}}$ (Fig. 4.4 and 6.6). In zero external field, H = 0, minimization of E with respect to θ_A yields the equilibrium canting angles

$$\theta_{1,2} = \cos^{-1}(\pm \frac{\Lambda \cdot m_A \cdot m_B}{2k_A}), \quad \text{(6. 8)}$$

which define the cone states depicted by the orientations 2, 3 and 1, 4 in Fig. 6.6, where $\theta_1 + \theta_2 = \pi$.

It should be noticed that the solutions $\theta_A = 0$ or π of $dE/d\theta_A = 0$ refer to maxima of E provided that $|\Lambda| < 2k_A/m_A \cdot m_B$. This is indeed, inferred from Mössbauer studies [Scho94a, Tapp98], where intermediate canting angles, $0 < <\theta_A> < \pi/2$, have been reported for Tb/Fe multilayers even at lowest temperatures. On the other hand, however, strong coupling, viz. $|\Lambda| \geq 2k_A/m_A \cdot m_B$, seems to follow from the fact that $<\theta_A>$ changes but weakly when applying perpendicular magnetic fields up to H = 4 MA/m at low T [Tapp98]. Very probably, in addition to the canting mechanism described by Eq. (6. 8), random local tilting of $\mathbf{m}_B$ out of the normal direction might cause similar tilting of $\mathbf{m}_A$ via strong coupling. The directional disorder in the Tb/Fe interfaces resembles that observed in sperimagnetic amorphous TbFe alloy systems due to random anisotropy mechanisms [Eyme88]. Thus being essentially in the strong coupling limit it seems justified to neglect decoupling of $\mathbf{m}_A$ and $\mathbf{m}_B$ by our probing field, H = 0.72 MA/m, and to assume $\theta_{1,2}$ to be constant while scanning a TC.

Eq. (6. 7) then yields

$$\tau(\alpha) = -\mu_0 \cdot H \cdot [m_A \cdot \cos(\alpha + \theta_A) \pm m_B \cdot \cos\alpha], \quad \text{(6. 9)}$$

with $\theta_A = \pm\theta_{1,2}$ defined by Eq. (6. 8). Vanishing torque, $\tau = 0$, is expected for angular positions

$$\cos\alpha = \pm\frac{\sin\theta_{1,2}}{\sqrt{1+(m_B/m_A)^2 + \Lambda \cdot m_B^2/k_A}} \tag{6. 10}$$

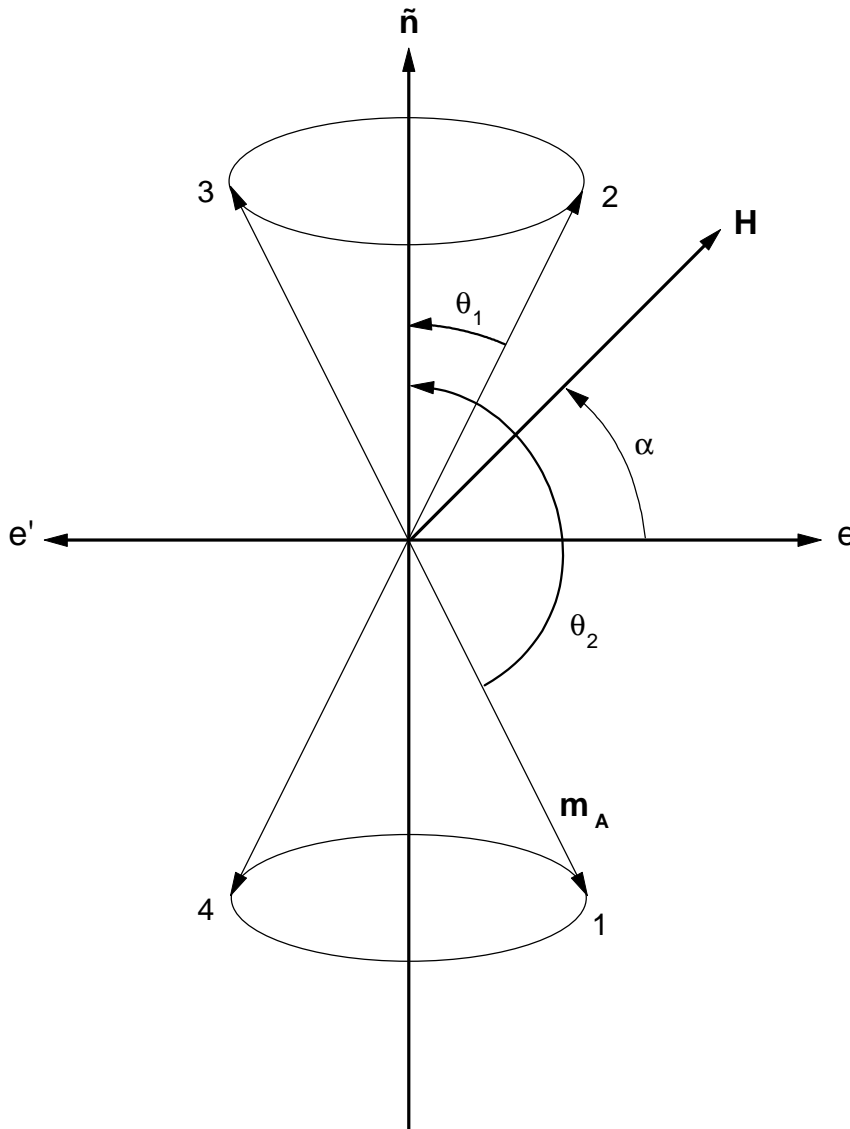*Fig. 6.6: Illustration of cone states referred to the measured TC of Y3 at T = 30 K (Fig. 6.3). θ_1 and θ_2 are the cone angles with respect to the film normal (see text).*

In the limit $m_B \rightarrow 0$ one obtains $\cos\alpha \approx \pm\sin\theta_{1,2}$, which leads to four different angles, $\alpha = \pm\theta_1 \pm \pi/2$. Hence, $\tau(\alpha)$ should vanish, whenever α coincides with one of the easy cone directions 1-4 (Fig. 6.6), where single domains of m_A are collinear with **H**. This result approximately

holds also at finite values of $\mathbf{m_B}$, in particular below the compensation temperature where the negative sign of Λ applies.

As can be seen in Fig. 6.3, however, this expectation is only partly met. Only two of the easy directions give rise to zero torque, $\tau \approx 0$, namely $\alpha = 270° + \theta_1$ (denoted as domain 1 in Fig. 6.6), $90° + \theta_1$ (domain 3) for the CCW and $\alpha = 90° - \theta_1$ (domain 2), $270° - \theta_1$ (domain 4) for the CW TC, where $\theta_1 \approx 30°$ in agreement with $\langle\theta\rangle$ data obtained on similar Tb/Fe multilayers [Mark98]. At a closer look, however, the missing easy directions are indicated by slight dips in both TCs (vertical arrows in Fig. 6.3). Obviously, the large field limit (see above) is not met in our experiment. Instead of being single domain the sample attains a multidomain structure with varying weight of the four possible easy directions. Full switching from, say, the lower to the upper cone state takes place only when $\mathbf{H}$ attains its extreme normal component in the vicinity of $\alpha = 90°$. That is why full alignment of $\mathbf{M}$ is not realized at $\alpha = 90° - \theta_1$ (domain 2), but in domain 3 upon rotating $\mathbf{H}$ first to $\alpha = 90°$ and then into its easy direction, $\alpha = 90° + \theta_1$. The CCW curve in Fig. 6.3 is thus understood by hysteretic switching between the domains 1 and 3, where $\tau \geq 0$ at any angular position. The domains 2 and 4 are only partly populated at intermediate angles (see above). When changing the sense of scanning, the torque changes sign such that $\tau \leq 0$ at any value of α. In the CW curve, hence, switching takes place between the fully aligned domains 2 and 4, whereas 1 and 3 are only partly aligned when hitting their respective easy directions. The smoothness of the observed TCs clearly indicates absence of sharp switching processes. Very probably nucleation and domain growth take place on a microscopic scale. Hence, the total torque observed will be a weighted superposition of four $\tau(\alpha)$ curves according to Eq. (6. 10), the micromagnetic model of which is presently not available.

The preceding discussion also provides some understanding of the peculiar mutual shifts between the CCW and CW TCs observed on Y1 and Y2 at $T < 100$ K (Fig. 6.1 and 2). Obviously in these cases, again, cone states are realized in the bulk of their Fe layers. Assuming smaller values $|\Lambda \cdot m_B/m_A|$ than in the case of the strongly uniaxial Y3 sample (Fig. 6.3), intraplanar anisotropy prevails in these cases. In the situation met, e. g., for Y1 at $T = 15$ K in Fig. 6.1 we assume $\theta_1 \approx 75°$. Upon rotating $\mathbf{H}$ in CCW direction switching takes place preponderantly between the nearly planar domains 1 and 3 with $\tau(\alpha) = 0$ at $\alpha = 90° + \theta_1$ and $270° + \theta_1$. Conversely the CW torque signal vanishes when hitting the easy directions 2 and 4

at $\alpha = 90° - \theta_1$ and $270° - \theta_1$. Owing to sufficiently large uniaxial anisotropy, $k_B > 0$, switching between domains 1 and 2 (3 and 4) is delayed. This explains the positive bias superimposed to the CCW TC, while it becomes negative when scanning into the CW direction. Remarkably, the largest angular hysteresis is found at $\alpha = 90$ and $270°$ in all cases shown in Fig. 6.1 and 2. In the vicinity of these angles hysteresis survives even at temperatures as high as T = 150 K in Y1.

6.1.4. Summary

Our investigations have shown that the two different Tb/Fe interfaces, rough (bottom, Fe-on-Tb, Y1) and smooth (top, Tb-on-Fe, Y2), respectively, induce PMA by different amounts. The appearance of hysteresis in the vicinity of $\alpha = 0, 180°, 360°, \cdots$, in the TCs of Y2 at T < 100 K (Fig. 6.2) is the key issue indicating stronger PMA in Y2 than in Y1. This is readily understood within the framework of our cone state model. Eq. (6. 8) indicates decreasing PMA for increasing θ_1, hence, decreasing m_B, if Λ, m_A and k_A are considered as constants. Indeed, in the case of rough interfaces encountered in Y1, the Fe atoms are distributed in a relatively large volume of an amorphous TbFe alloy. Hence, only a small fraction of them exhibits direct exchange interaction with the adjacent α-Fe layer. This explains the fairly large low-T cone angle, $\theta_1 = 75°$, in Y1 compared to those in Y2, $\theta_1 = 66°$, or in Y3, $\theta_1 \approx 30°$ (Fig. 6.1-3)

Contrastingly with these low-T observations the decrease of τ_{max} between T = 300 and 250 K is substantially larger in Y1 (6%) than in Y2 (2%). Hence, in this temperature range PMA evolves more effectively in Y1 than in Y2. Very probably this is a consequence of interface alloying. In Y1 this enhances the ferrimagnetic ordering temperature compared to that of pure Tb, 219 K, above which PMA is virtually suppressed in Y2. This is corroborated by evaluating TCs recorded at various fields, 480 kA/m $\leq$ H $\leq$ 720 kA/m, at room temperature. Using the relationship for the inverse slope at $\alpha = 0$ or $180°$ [Andr61]

$$\frac{d\alpha}{d\tau} = \frac{1}{\mu_0 \cdot V \cdot M_S \cdot H} + \frac{1}{2 \cdot V \cdot K_{eff}} + \frac{1}{D}, \qquad (6.\ 11)$$

where D is the torsion constant of the torsion fiber, we obtain M_S = 956, 985, 1012 kA/m and

$K_U = K_{eff} - \dfrac{\mu_0}{2} \cdot M_S^2$ = 1.70, 1.07, 2.51·10^5 J/m^3 for Y1, Y2 and Y3, respectively. Here an

effective single layer model is assumed and K_U refers primarily to the interface PMA. M_S, which refers to the total volume V of the multilayers, is virtually independent of their kind. In contrast, the K_U values differ considerably, being lowest in Y2, intermediate in Y1 (thanks to interface alloying), and largest in Y3 (owing to additional coupling, see below). The observed canting angles, <θ> = 79.1, 75.9, 70.4° [Tapp98] are in qualitative agreement with these assertions.

PMA due to coupling with both top and bottom interfaces is much more pronounced in Y3 multilayers (Fig. 6.3). Large effects are already observed when cooling from RT to 200 K, probably due to the ferrimagnetic polarization in the rough bottom interfaces. Even more spectacular effects occur upon cooling further down to 30 K, where the smooth top layers are assumed to play a major role. In addition, the overall PMA becomes enhanced by dipolar coupling of the α-Fe layers via the intercalated magnetic Tb layers. A similar mechanism was proposed to be active in other rare earth-transition metal multilayers like CeH$_2$/Fe [Schu95a].

6.2. Fe/Tb multilayers with Ag layers

Fig. 6.7 shows the SQUID magnetization curves M(H) (a, c) and the polar Kerr ellipticity ε_K(H) (b, d) measured on Ag1 (a, b) and Ag2 (c, d) at room temperature (RT). Although the sharp switching-behavior of the in-plane M(H) curves (1) of Ag1 (a) and Ag2 (c) indicate that the spontaneous magnetization lies in the film plane, the corresponding polar M(H) curves (2) differ from ordinary hysteresis loops reflecting mere in-plane anisotropy. They reveal superpositions of two different magnetization reversal processes as evidenced by changes of the slope, dM/dH, at |H| ≤ 0.2 MA/m. A tentative decomposition of each of these curves into one curve saturating at H_s ≈ 1 MA/m (2a) and another one saturating at H_s ≈ 0.3 MA/m (2b) is shown for both samples Ag1 (a) and Ag2 (c). It seems plausible that the former refers to in-plane magnetized crystalline α-Fe. Its H_s value is reduced from the bulk value M_s = 1.76 MA/m to the observed one owing to the large volume of (nearly) non-magnetic Ag and Tb taking into account a demagnetizing factor N ≈ 1. As will be outlined below the hysteresis

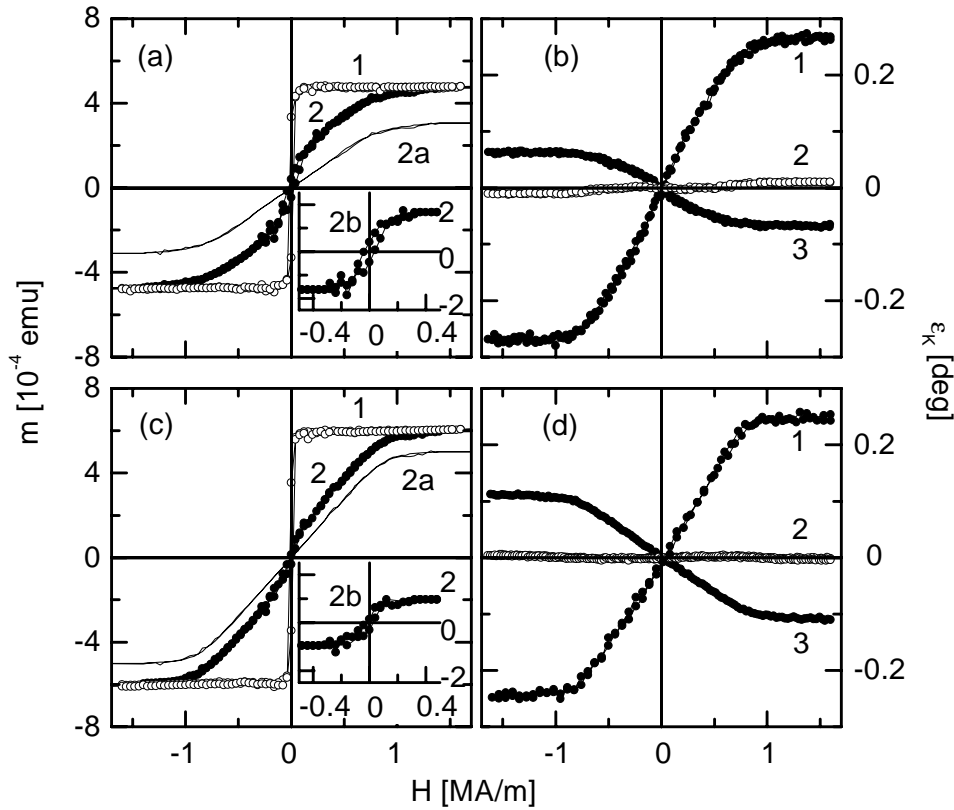*Fig. 6.7a, c: SQUID magnetization curves of (a) Si/[Tb(1.4 nm)/Fe(3.5)/Ag(5.0)]₁₀ (=Ag1) and (c) Si/[Fe(3.5)/Tb(1.4)/Ag(5.0)]₁₀ (=Ag2) measured in in-plane (1) and polar (2) geometry at T = 300 K, respectively. The polar curves (2) are decomposed into components with in-plane (2a) and perpendicular anisotropy (2b, inset).*

b, d: Polar Kerr ellipticity (ε_K) hysteresis loops obtained at T = 285 K and wavelengths λ = 300 (1), 550 (2) and 600 nm (3), and λ = 300 (1), 575 (2) and 700 nm (3) on Ag1 (b) and Ag2 (d), respectively.

curves (2b) are due to amorphous FeTb alloys growing at the interfaces between the Fe and Tb layers. They exhibit preponderantly perpendicular anisotropy even at room temperature.

Comparison of the curves (2b) shows that both remanence, M_r, and coercivity, H_c, are larger for Fe-on-Tb (Ag1) than for Tb-on-Fe (Ag2). This becomes much clearer upon cooling to T = 50 K (Fig. 6.9). Whereas Ag1 (curve 2 in Fig. 6.9a) reveals a nearly rectangular polar loop indicating strong PMA with a high ratio of $M_r/M_s \approx 0.85$ (M_s = saturated magnetization), the polar loop of Ag2 (curve 2 in Fig. 6.9c) is strongly inclined and reveals a low ratio of $M_r/M_s \approx$ 0.23. This is also evidenced by the in-plane M(H) curves 1 in Fig. 6.9a and c, which are more
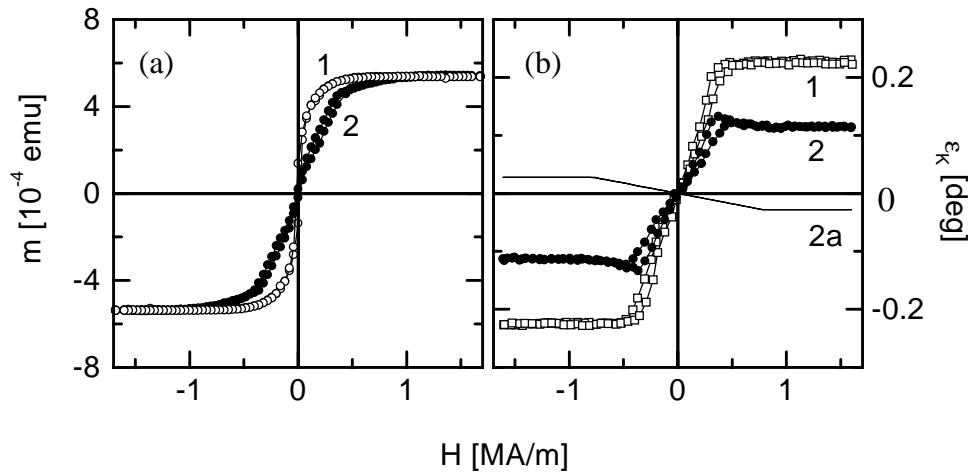
Fig. 6.8a: SQUID magnetization curves of Si/[Tb(1.4 nm)/Fe(3.5)]$_{10}$ (=Ag3) measured in in-plane (1) and polar (2) geometry at T = 300 K, respectively. b: Polar Kerr ellipticity (ε_K) hysteresis loops obtained at T = 285 K and wavelengths λ = 550 (1) and 850 nm (2) on Ag3. Curve 2a is calculated from curve 2 by subtracting curve 1 properly weighted

rectangular for Ag2 than for Ag1. Interestingly, in both cases the polar coercive fields are quite similar, $H_c \approx 0.13$ and 0.07 MA/m for Ag1 and Ag2, respectively (Fig. 6.9), whereas a ML without any Ag layers, Ag3, shows much larger coercivity, $H_c \approx 0.46$ MA/m (Fig. 6.10a, curve 2). It is not at all surprising that considerable PMA is retained in this sample up to room temperature as shown by the polar curve 2 in Fig. 6.8a.

The different amounts of PMA observed on the samples Ag1 and Ag2 are readily explained by the structural differences of their Tb/Fe interfaces [Rich96a]. Whereas Fe-on-Tb in Ag1 is subject to interface alloying (rough interface) and therefore exhibits ferrimagnetism with large uniaxial anisotropy already at RT, the Tb-on-Fe interfaces in Ag2 are essentially smooth. They exhibit ferrimagnetic coupling only below the ordering temperature of Tb, T_c = 219 K. Finally, the drastic increase of PMA in the absence of diamagnetic blocking layers in the Ag3 system is a consequence of interlayer exchange coupling of the Fe layers via antiferromagnetically coupled Tb layers. Whereas only a small fraction of the isolated Fe layers (viz. their interfaces with adjacent Tb layers) carries PMA at room temperature (Fig. 6.7a, c), virtually the entire sample is perpendicularly polarized in the presence of interlayer exchange (Fig. 6.8a) or, more pronounced, in the low T regime (Fig. 6.10a). This is consistent with CEMS data revealing the average canting angle $<\theta_{Fe}>$ between the film normal and the

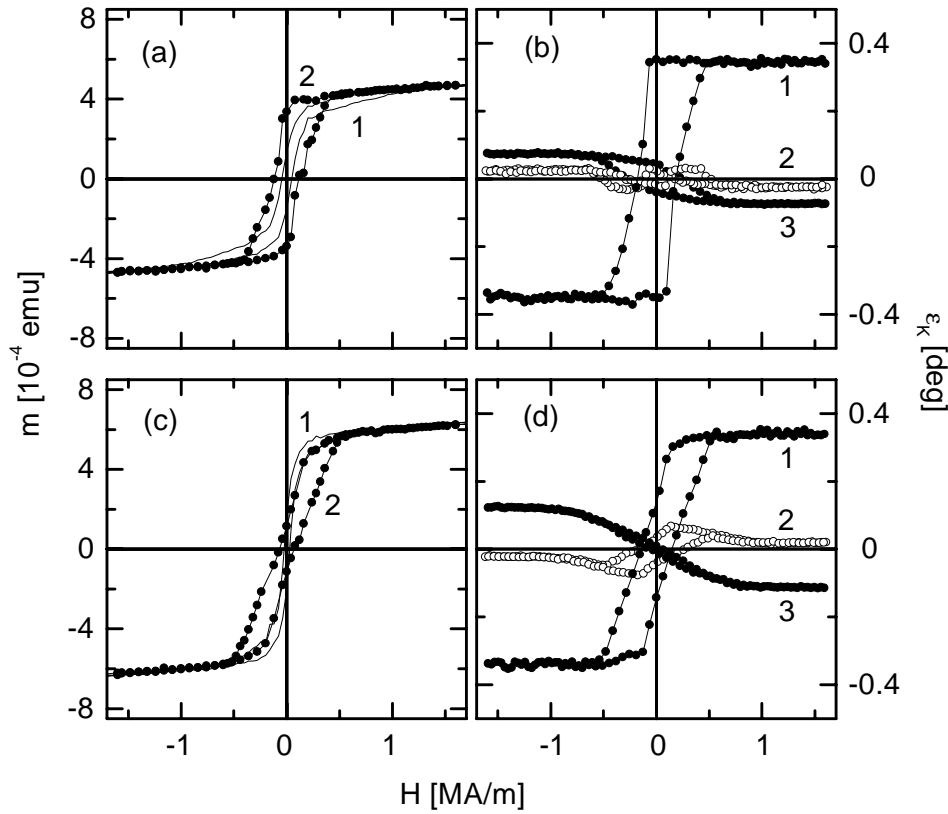*Fig. 6.9a, c: SQUID magnetization curves of (a) Si/[Tb(1.4)/Fe(3.5)/Ag(5.0)]₁₀ (=Ag1) and (c) Si/[Fe(3.5)/Tb(1.4)/Ag(5.0)]₁₀ (=Ag2) measured in in-plane (1) and polar (2) geometry at T = 50 K, respectively. b, d: Polar Kerr ellipticity (ε_K) hysteresis loops obtained at T = 50 K and wavelengths λ = 300 (1), 550 (2) and 600 nm (3), and λ = 300 (1), 575 (2) and 700 nm (3) on Ag1 (b) and Ag2 (d), respectively.*

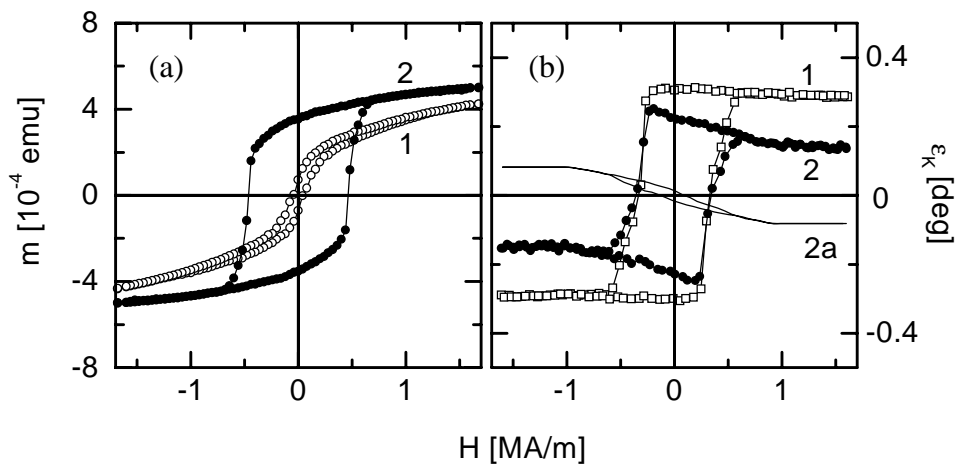*Fig. 6.10a: SQUID magnetization curves of Si/[Fe(3.5)/Tb(1.4)]₁₀ (=Ag3) measured in in-plane (1) and polar (2) geometry at T = 50 K, respectively. b: Polar Kerr ellipticity (ε_K) hysteresis loops obtained at T = 100 K and wavelengths λ = 550 (1) and 850 nm (2) on Ag3. Curve 2a is calculated from curve 2 by subtracting curve 1 properly weighted.*

direction of the Fe spins to change gradually from about 90° for Ag1 and Ag2, and 43° for Ag3 at T = 300 K to 31 ⋯ 35° at T = 80 K for all samples [Mark98].

Deeper insight into the individual properties of the MLs is gained from their magneto-spectroscopical properties at low temperature. As shown in Fig. 6.9b and d, the shapes of the polar $\varepsilon_K(H)$ curves strongly depend on the wavelength used. For $\lambda = 300$ nm (curves 1) they resemble the corresponding M(H) curves (Fig. 6.9a and b). A closer look, however, reveals a higher degree of rectangularity in $\varepsilon_K(H)$. As will be discussed below this hints at spectroscopic selection of a particular subsystem with enhanced PMA. With increasing wavelength $\varepsilon_K(H)$ changes its sign. This is corroborated by the low-T Kerr spectra, $\varepsilon_K(\lambda)$, in Fig. 6.11a (curves 1 and 2) recorded at wavelengths ranging between 275 and 900 nm. Surprisingly, this behavior is not a mere spectroscopic effect. From the $\varepsilon_K(H)$ curves in Fig. 6.9b and d at $\lambda = 600$ and 700 nm, respectively (curves 3), drastic changes of the hysteresis cycles become obvious. They are less rectangular and indicate considerably larger saturation fields, $H_s \approx 0.8$ MA/m, than the cycles recorded at $\lambda = 300$ nm. It is noticed from the curves 3 that different coercive fields $H_c \approx 0.25$ and 0.05 MA/m are active in Ag1 and Ag2, respectively.

The different shapes of M(H) and $\varepsilon_K(H)$ indicate magnetic heterogeneity of the multilayers, which is differently weighted by the experimental methods involved. By definition, SQUID magnetometry measures the total moment and thus yields an average magnetization weighted by volume fractions. Contrastingly, Kerr magnetometry averages by spectroscopical weight when disregarding multilayer interference effects. These are virtually negligible in the ultrathin period limit [Višn95]. Obviously the positive UV response at 300 nm is sensitive to a subsystem with large PMA, whereas the negative response reflected by the red light spectrum probes a subsystem with weak PMA. Both of these extremes may be superimposed with appropriate weight factors in order to construct either the average magnetization curves, M(H) (Fig. 6.9a and c), or the $\varepsilon_K(H)$ curves taken at intermediate wavelengths. This has been performed explicitly on the curves 2 in Fig. 6.9b and d, which were recorded at 550 and 575 nm, respectively. Very clearly they reflect both the steep rectangularity of the UV response in weak fields and the negative tail towards gradual saturation typical of the response in the red spectral region. Best-fit procedures suggest the following superpositions: $\varepsilon_K(\lambda_0) = a \cdot \varepsilon_K(\lambda_a) + b \cdot \varepsilon_K(\lambda_b)$ with $\lambda_a = 300$ nm, $\lambda_b = 600$ (700) nm, a/b = 0.16 (0.42) for Ag1 (Ag2) at $\lambda_0 = 550$ (575) nm. Similarly, the virtually vanishing Kerr signal, $\varepsilon_K(\lambda_0) \approx 0$, observed at T = 300 K

(Fig. 6.7b and d, curves 2) can be constructed using a/b = 0.28 and 0.22 for Ag1 and Ag2, respectively.

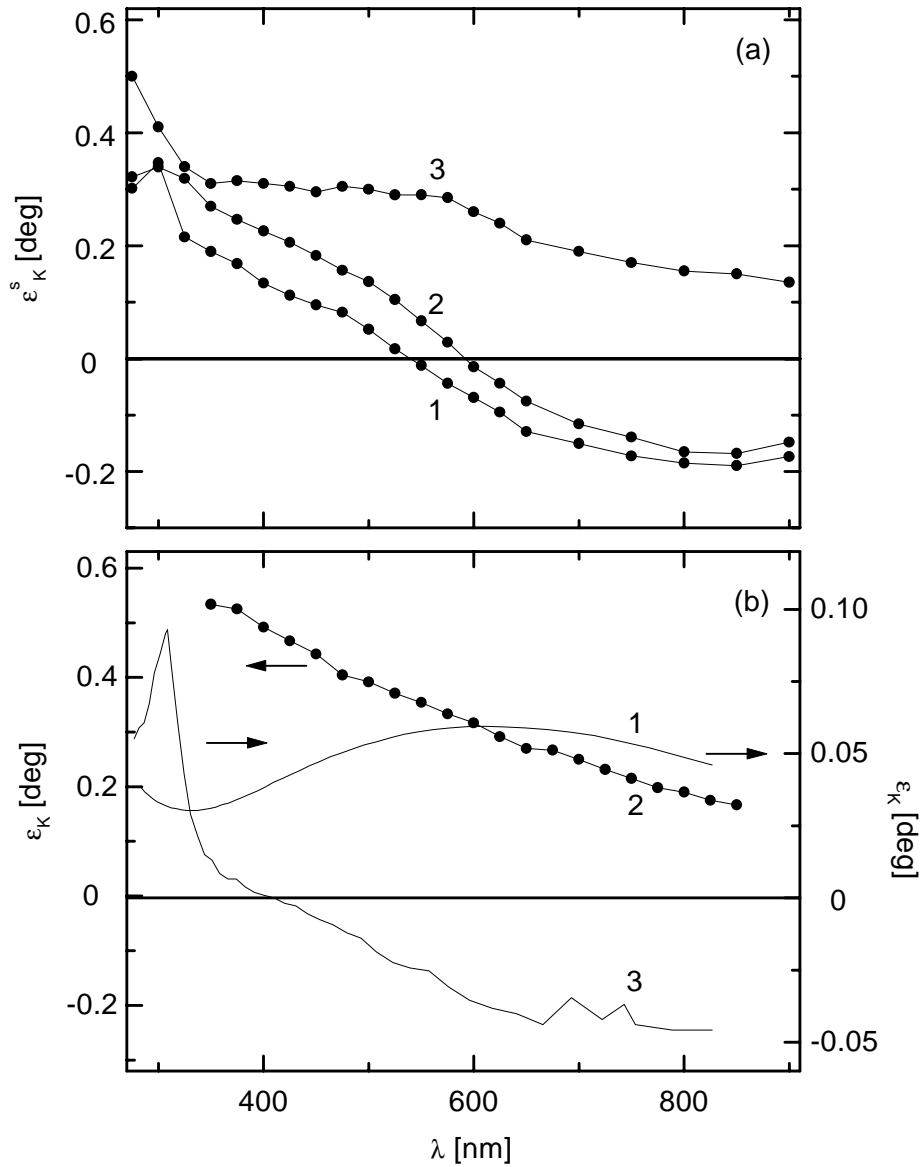Fig. 6.11a: Saturated polar Kerr ellipticity (ε_K^s) spectra obtained on (1) Si/[Tb(1.4)/Fe(3.5)/ Ag(5.0)]$_{10}$ (=Ag1), (2) Si/[Fe(3.5)/Tb(1.4)/Ag(5.0)]$_{10}$ (=Ag2) at T = 50 K and (3) Si/[Fe(3.5)/ Tb(1.4)]$_{10}$ (=Ag3) at T = 100 K for wavelengths 275 ≤ λ ≤ 900 nm. b: Polar Kerr ellipticity spectrum of bcc Fe (curve 1, [Krin65]), amorphous [Fe(1.5)/ Tb(1.9)]$_{20}$ (2) and [Fe(3.5)/Ag(6.0)]$_5$ (3, [Kris93]).

At the first glance the negative-valued ε_K spectrum might be taken as characteristic of the Fe/Ag interfaces encountered in the samples Ag1 and Ag2. This seems to be corroborated by the Kerr spectrum of the related ML system [Fe(3.5)/Ag(6.0 nm)]$_5$ [Kris93]. It exclusively

contains Fe/Ag interfaces and shows a change of sign at intermediate wavelengths similarly as observed on Ag1 and Ag2 (Fig. 6.11b, curve 3). However, this simple interpretation must be ruled out, when considering the sample Ag3, which contains no Fe/Ag interface at all. Its $\varepsilon_K(H)$ curve recorded at $\lambda = 850$ nm (Fig. 6.10b, curve 2) reveals, again, signatures of two hysteresis cycles. Subtracting a dominating rectangular part in proportion to $\varepsilon_K(H)$ recorded at $\lambda = 550$ nm (Fig. 6.10b, curve 1), one ends up, again, at a negative loop reflecting soft behavior ($H_c \approx 0.8$ MA/m) and weak hysteresis (Fig. 6.10b, curve 2a). It closely resembles the curves 3 measured on Ag1 and Ag2 (Fig. 6.9b and d). It appears, hence, tempting to assume that all of the negative ε_K signals referring to long wavelengths have the same origin as will be justified in the following.

First of all, since Ag3 does not contain any Fe/Ag interfaces and [Fe(3.5)/Ag(6.0 nm)]$_5$ [Kris93] lacks any Tb/Fe interfaces, it is argued that the soft magnetic subsystem must be found distant from the immediate interfacial regions. At this point a structural peculiarity of evaporated Tb/Fe MLs has to be recalled. It is well-known [Dufo91] that Fe grows in an amorphous modification, a-Fe, up to a single layer thickness $t_{Fe}^{cr} \approx 2.0$ nm, whereas it crystallizes into the bcc modification at $t_{Fe} > t_{Fe}^{cr}$. Remarkably, however, a certain fraction corresponding to a layer with about 0.6 nm thickness remains amorphous [Dufo91]. Excluding monoatomic layers of a-Fe adjacent to Tb and/or Ag, there is still a-Fe left in the „bulk" of each Fe layer corresponding to 1-2 monolayers. Its very existence has recently been corroborated by Mössbauer spectroscopy on ^{57}Fe probe layers within a sample similar to Ag3 (see below [Jung94]). Its exact location within the layer is unknown. However, its spectroscopic importance in all MLs with $t_{Fe} = 3.5$ nm seems to be unmistakable. It distorts the Kerr spectroscopic hysteresis loops heavily by virtue of „soft" contributions with inverted sign (Fig. 6.9b, d, curves 3, and Fig. 6.10b, curve 2).

When assigning the soft contribution to a-Fe a comparison with the spectral properties of Tb/Fe MLs containing exclusively a-Fe seems in order. To this end we prepared a sample of [Fe(1.5 nm)/Tb(1.9 nm)]$_{20}$ ($\equiv$ HT ML with $t_{Fe} = 1.5$ nm, HT15, see Chap. 5) and recorded its Kerr ellipticity spectrum, $\varepsilon_K^s(\lambda)$, at saturation (Fig. 6.11b, curve 2). It is seen that ε_K^s decreases with increasing wavelength in a similar manner as observed on Ag1 and Ag2 (Fig. 6.11a, curves 1 and 2), thus sharply contrasting the nearly constant Kerr signal of α-Fe (Fig.

6.11b, curve 1 [Krin65]). However, negative values of ε_K^s are never attained in the spectral region considered. We are, hence, inclined to attribute this spectral feature to a special morphology of a-Fe, which is very probably not layer-like as HT15. We rather propose that a-Fe clusters adjacent to grain boundaries and voids, being magnetically decoupled from the crystallized Fe films, might be responsible for the observed magnetic and spectroscopic heterogeneity. Here we give some arguments supporting our hypothesis.

(i) A segregated a-Fe phase consisting of separate clusters does not inhibit ferromagnetic coupling between adjacent layers, whereas a layer-like a-Fe component would necessarily couple to the remainder of the ML, at least at low temperatures.

(ii) Mössbauer spectroscopy on 0.5 nm thick ^{57}Fe probe layers within a ML of [Fe(4.0 nm)/Tb(1.9 nm)]$_{30}$ reveals the largest fraction of a-Fe in the central parts of the Fe layers [Jung94]. Hence, uncrystallized iron is not restricted to the interface regions as would have been anticipated from a pseudomorphic recrystallization model.

(iii) In contrast with „bulk" a-Fe [Alpe76, Rich96b] the novel segregated phase seems to be ferromagnetic at room temperature. This is shown by the characteristic shape of the Kerr optical hysteresis curve recorded at λ = 850 nm on Ag3 in Fig. 6.8b (curve 2). Subtraction of a „hard" component in proportion to the λ = 550 nm curve 1 reveals a „soft" component (curve 2a) with properties being close to the low-T ones (Fig. 6.9b, d and Fig.6.10b, curves 3 and 2a, respectively).

(iv) The low saturation field value, $H_s \approx$ 0.8 MA/m, probably reflects a demagnetization factor being significantly smaller than unity (N = 1/3 for spherical particles) and coupled to a saturation magnetization close to that of α-Fe (M_s = 1.8 MA/m).

Finally, a remark on the magnetic relevance of the soft magnetic a-Fe component seems in order. When inspecting the polar magnetization curve 2 in Fig. 6.10a, its rounded shape in the low-field region seems to hint at a superposition of a sharp rectangular „hard" component and a smooth „soft" one, similar to that assigned to the MOKE curve 2 in Fig. 6.10b (except for the different signs of the soft components). However, according to Mössbauer spectroscopy on a sample similar to Ag3 (see above [Tapp98]) the rounded shape of M(H) is primarily due to field-induced fanning of the Fe moments. Their canting angle $<\theta_{Fe}>$ gradually increases upon decreasing the field from, say, positive values to -H_c, before they flip into the reverse direction at H < -H_c. This peculiarity is due to the ferrimagnetic coupling between Fe and Tb moments at sufficiently low temperatures [Eyme88]. It should be noticed that the field-

induced fanning effects of the latter ones must also be accounted for in a complete analysis [Tapp98]. Additional rounding of the magnetic hysteresis due to the MOKE „active" soft a-Fe component is probably much smaller than the above discussed fanning contribution. Estimating an effective 0.2 nm thickness per single Fe layer [Dufo91] a contribution amounting to 5 - 10% of the total M_s value may be anticipated. Hence, at most about 20% of the observed rounding in the low-field regime of curve 2 in Fig. 6.10a might be due to the uncoupled a-Fe phase.

In conclusion, MLs of Fe/Ag/Tb, Fe/Ag/Tb and Tb/Fe are shown to contain a novel soft-magnetic component, which is virtually decoupled from the ML. Presumably being due to a-Fe segregated within the α-Fe layers it can be isolated by means of its negative Kerr ellipticity in the near infrared, where other Fe modifications and alloys contribute but weakly. Thus in a unique way, never before observed in the 1eV photon energy range, component selectivity is achieved with a quality close to that of core state magneto-spectroscopy, e. g. XMCD [Eber96]. In view of the unavoidable a-Fe components in as-evaporated MLs it will be interesting to investigate epitaxial Tb/Fe MLs lacking such components and exhibiting enhanced PMA.

Furthermore it is shown that the Fe/Ag interfaces lower the PMA, which is primarily induced by Fe/Tb interfaces and increases with decreasing temperature. In particular the exchange coupling, which strongly enhances the PMA in Fe/Tb MLs, is suppressed by virtue of diamagnetic blocking layers of Ag. Owing to enhanced interface alloying the rough Fe-on-Tb interfaces are stronger sources of PMA than the sharp Tb-on-Fe ones.